Multispectral Bathymetry Using a Simple Physically Based Algorithm

David R. Lyzenga, Norman P. Malinas, and Fred J. Tanis

***Abstract*—A simple method for estimating water depths from multispectral imagery is described and is applied to several IKONOS data sets for which independent measurements of the water depth are available. The methodology is based on a physical model for the shallow-water reflectance, and is capable of correcting for at least some range of water-quality and bottom-reflectance variations. Corrections for sun-glint effects are applied prior to the application of the bathymetry algorithm. The accuracy of the depth algorithm is determined by comparison with ground-truth measurements, and comparisons between the observed and calculated radiances are presented for one case to illustrate how the algorithm corrects for water-attenuation and/or bottom-reflectance variations.**

***Index Terms*—Multispectral scanners, ocean optics, remote sensing, water depth.**

I. Introduction

THERE IS AN obvious need for measurements of water depth, particularly in shallow areas that may present a risk to navigation. These areas are subject to rapid changes due to erosion and deposition, especially during storms. Shallow water poses difficult problems for conventional ship sounding techniques because of the difficulties in navigating in shallow water and the high spatial sampling rates required. Because of these considerations, remote-sensing techniques are attractive, provided that reliable depths can be estimated from the remote-sensing data.

The problem of estimating water depths from remote-sensing data has a relatively long history, this being one of the applications of multispectral scanner technology that were envisioned shortly after the development of this technology in the 1960s. However, the recent commercial availability of data from high-resolution spaceborne multispectral scanners such as IKONOS [1] and the development of hyperspectral sensors with a large number of wavelength bands [2], [3] have provided a new impetus for revisiting this subject. In this paper, we review the physical or theoretical basis for the measurement and present new results derived from several IKONOS data sets.

It must be noted that advances in other types of remote-sensing technology have also been made in recent years. We note, in particular, the development of light detection and ranging (LIDAR) bathymetric techniques such as the Scanning Hydrographic Operational Airborne LIDAR System (SHOALS) owned and operated jointly by the U.S. Army Corps of Engineers and the U.S. Navy [4]. This system represents a much more direct measurement of the water depth, being the optical equivalent of acoustic depth sounding, and is capable of providing accurate depth measurements over wide areas in much less time than could be done by ship surveys. In fact, these measurements are used as "ground truth" for the IKONOS data sets analyzed in this paper. Our motivation for continuing the development of passive multispectral techniques is that the cost of operating the SHOALS system is still relatively high, and it is not yet practical to deploy this system in all areas of the world where updated bathymetric information is required or desired.

Manuscript received March 29, 2005; revised November 3, 2005.

D. R. Lyzenga and N. P. Malinas are with the General Dynamics Advanced Information Systems Division, Ann Arbor, MI 48197 USA (e-mail: david.lyzenga@gd-ais.com).

F. J. Tanis is a consultant residing in Bend, OR USA (e-mail: tanisfred@hotmail.com).

Digital Object Identifier 10.1109/TGRS.2006.872909

II. Shallow-Water Reflectance Model

The water-depth-estimation algorithm described in this paper is based on a simplified model for the reflectance of shallow-water areas. The model represents an approximation to the radiative transfer solution in water and is therefore not completely accurate, but we believe that the modeling error is small compared with the uncertainties in the parameters entering the model. According to this model, the subsurface reflectance for a water depth h can be written as

$$R(h) \equiv \frac{\pi L^-}{E_i^-} = r_{\rm v} + r_{\rm b}^* e^{-\alpha h} \tag{1}$$

where E_i^- is the downwelling irradiance and L^- is the upwelling radiance just below the surface, $r_{\rm v}$ is the reflectance due to volume scattering in the water column for an effectively infinite water depth, $r_{\rm b}^* = r_{\rm b} - r_{\rm v}$, where $r_{\rm b}$ is the bottom reflectance, and α is the sum of the diffuse attenuation coefficients for upwelling and downwelling light. This model has been derived in different ways and used in slightly different forms by several investigators [5]–[8]. The parameters in this model can be related to the inherent optical properties of the water and the bottom, but in our case, they are empirically derived by a comparison of remote-sensing signals with measured depths.

The effect of the air–water interface is fourfold: 1) to reflect incident radiation (direct sunlight and diffuse skylight) into the field of view of the sensor; 2) to reduce slightly the downwelling irradiance below the surface and concentrate this radiation into a smaller range of zenith angles; 3) to substantially reduce the upwelling radiance passing through the surface due to refractive effects; and 4) to internally reflect some of the upwelling radiance back downward, causing it to undergo further scattering or reflection from beneath the surface. The first three of these effects modify the magnitude of the terms

in (1) but do not modify the form of this equation. Internal-reflection effects are important only for very shallow water, and are neglected here. Thus, the upwelling radiance above the surface can be written as

$$L(h) = L_{\mathrm{s}} + L_{\mathrm{b}} e^{-\alpha h} \tag{2}$$

where L_{s} includes surface-reflection as well as volume-scattering effects, and L_{b} includes transmission losses through the air–water interface as well as the bottom reflectance and volume-scattering effects included in r_{b}^{*}. Surface-reflection effects are discussed further in Section III.

To complete the picture, we must include the effects of the atmosphere on the measured radiance. Similar to surface-reflection effects, these include an additive term due to path radiance, i.e., scattering of sunlight by aerosols and molecular constituents, and a multiplicative factor due to transmission losses in the atmosphere. These effects can also be absorbed into the L_{s} and L_{b} terms in (2), so the form of this equation is not changed.

III. Sun-Glint-Correction Algorithm

In some cases, if the atmosphere and water optical properties are sufficiently uniform, and the solar angles and view geometry is such that a minimal amount of direct sunlight is reflected into the field of view, the L_{s} term in (2) may be considered a constant. In such cases, this term can be determined empirically by simply averaging the signals over optically deep water. In general, however, there may be variations in L_{s} due to sun glint, haze or thin clouds, or water-quality fluctuations. Many of these variations (at least from the first two sources) can be corrected if the multispectral scanner data include a near-infrared (NIR) channel. The reflected sunlight (i.e., the sun glint) contribution to L_{s} can be written as

$$L_{\mathrm{sg}} = c(\lambda) p(\eta_{xs}, \eta_{ys}) \tag{3}$$

where $c(\lambda)$ is a wavelength-dependent factor that includes the Fresnel reflectance of the surface and the spectral intensity of the incident sunlight, and $p(\eta_{xs}, \eta_{ys})$ is the surface slope probability density function evaluated at the slopes required for specular reflection of the sunlight into the sensor field of view, i.e., $\eta_{xs} = -n_x/n_z$ and $\eta_{ys} = -n_y/n_z$, where n_x, n_y, and n_z are the components of the surface normal vector $n = (k_s + k_o)/|k_s + k_o|$, in which k_s and k_o are vectors pointing toward the sun and the observer (sensor), respectively. This equation implies that there is a correlation of the sun-glint signal between wavelength bands, since the factor $p(\eta_{xs}, \eta_{ys})$ is the same for all bands. The wavelength dependence can be determined empirically by isolating a deep-water area containing sun-glint patterns and computing the covariance of each band relative to the NIR band, i.e.,

$$\rho_{ij} = \frac{1}{N}\sum_{n=1}^{N} L_{in} L_{jn} - \frac{1}{N}\sum_{n=1}^{N} L_{in} \frac{1}{N}\sum_{n=1}^{N} L_{jn} \tag{4}$$

where L_{in} is the nth sample of the radiance in band i. The coefficient relating the sun-glint signal in band i to that in the NIR channel (band j) is then given by

$$r_{ij} = \frac{\rho_{ij}}{\rho_{jj}}. \tag{5}$$

The correction is applied by scaling the NIR signal by this factor and subtracting from the band under consideration, i.e.,

$$L_i' = L_i - r_{ij}(L_j - \overline{L}_j) \tag{6}$$

where $\bar{L}_j$ is the mean radiance in the NIR channel. The reason that the NIR channel is used for this correction is that there is practically no volume scattering or bottom-reflected signal in this channel, so the correction can be applied over the entire scene without changing the depth dependence of the corrected signal.

A similar correction can be applied for variations in L_{s} due to haze or thin clouds, by computing the covariance over a deep-water region containing these variations. However, the correction coefficients will, in general, be different for atmospheric effects than for sun glint, so a correction can only be made for one or the other of these effects. If the deep-water area contains both sun glint and atmospheric variations, the procedure outlined above will achieve a compromise correction for both types of effects, but the correction may not be exact for either effect.

IV. Depth-Estimation Algorithm

If the water optical properties and the bottom reflectance were uniform within a given region, (2) could be simply solved for the water depth, yielding a depth algorithm of the form

$$\hat{h} = \frac{1}{\alpha}\ln(L_{\mathrm{b}}) - \frac{1}{\alpha}\ln(L' - L_{\mathrm{s}}') \tag{7}$$

where $\hat{h}$ is the estimated depth, L' is the radiance corrected for sun glint and/or atmospheric variations, and L_{s}' is the average deep-water signal after this correction. In most cases, however, there are variations in the bottom reflectance and/or water optical properties that lead to errors in the depth estimated using (7). These errors can in some cases be reduced by means of multispectral algorithms. For example, given N spectral bands, we can define the linear combinations

$$Y_i = \sum_{j=1}^{N} A_{ij} X_j \tag{8}$$

where $X_j = \ln(L_j' - L_{sj}')$ and A_{ij} are elements of the rotation matrix defined by Lyzenga [6]. If the water optical properties are uniform, it can be shown that the first $N-1$ of these linear combinations are independent of the depth, while the last one (Y_N) is a function of both the water depth and the bottom reflectance. The variables Y_1 to Y_{N-1} can therefore be considered as depth-invariant indexes of the bottom type. It is reasonable to hypothesize that a correction for bottom-reflectance variations can be expressed as a linear combination

of these bottom-type indexes, and to propose a depth algorithm of the form

$$\hat{h} = h_o - \sum_{j=1}^{N} h_j X_j. \tag{9}$$

Such an algorithm was in fact applied quite successfully to an airborne multispectral data set in which the h_j parameters were determined by a regression analysis using a set of depths measured by an LIDAR system operated simultaneously with the multispectral scanner [9].

Although this algorithm was derived under the assumption that the water optical properties are uniform, it can be shown that the depths obtained from (9) are insensitive to certain types of variations in the water-attenuation coefficients as well as the bottom reflectance. To see this, we note that, using the model expressed by (2), the X_j variables can be written as

$$X_j = \ln(L_{\mathrm{b}j}) - \alpha_j h + \varepsilon_j \tag{10}$$

where $L_{\mathrm{b}j}$ is proportional to the bottom reflectance in band j, α_j is proportional to the water-attenuation coefficient in this band, h is the actual water depth, and ε_j represents random noise in the measurement. Substituting this into (9), and neglecting the noise term, yields the estimated depth

$$\hat{h} = \left(h_o - \sum_{j=1}^{N} h_j \ln(L_{\mathrm{b}j}) \right) + \left(\sum_{j=1}^{N} h_j \alpha_j \right) h. \tag{11}$$

The algorithm is properly "calibrated" if the first term in brackets is equal to zero, and the second term in brackets is equal to one, i.e., if

$$h_o = \sum_{j=1}^{N} h_j \ln(L_{\mathrm{b}j}) \quad \sum_{j=1}^{N} h_j \alpha_j = 1. \tag{12}$$

Clearly, this set of equations exactly determines the h_j parameters if $N = 1$ and underdetermines these parameters if $N > 1$, for a fixed set of $L_{\mathrm{b}j}$ and α_j. That is, if more than one channel is used, there is more than one set of parameters that will satisfy (12) for fixed $L_{\mathrm{b}j}$ and α_j. If $N = 2$, and if there are two different bottom types or two different water masses in the scene (but not both), then (12) can be solved, so that the correct depth will be estimated correctly for both. If $N > 2$, then (12) can be satisfied for two sets of bottom reflectances and attenuation coefficients, and so on. In fact, a range of the bottom reflectances and/or water-attenuation coefficients can often be accommodated, provided that (12) are satisfied over the entire range of values. For example, suppose we have a sensor with two bands and a scene that satisfies (12) with $h_1 = -h_2$. Then, it is easy to see that (12) will continue to be satisfied as long as $\alpha_1 - \alpha_2$ does not change and as long as $L_{\mathrm{b}1}/L_{\mathrm{b}2}$ remains constant. Thus, if there is a constituent that has a specific attenuation coefficient that is the same in both bands, variations in the concentration of this constituent will not affect the accuracy of the depth estimate. On the other hand, the specific attenuation coefficient of biogenic constituents such as chlorophyll and colored dissolved organic matter (CDOM) is a strong function of the wavelength, being much larger in the blue than in the green region of the spectrum. Variations in the concentration of such constituents will affect the value of $\alpha_1 - \alpha_2$ and will therefore cause depth errors if $h_1 = -h_2$. However, the impact of such variations on the depth algorithm can, in this case, be minimized by choosing

$$\sum_{j=1}^{N} h_j \alpha_j^* = 0 \tag{13}$$

where α_j^* is the specific attenuation coefficient of the variable constituent. Thus, although the depth algorithm expressed by (9) may not work in all cases, it can be tailored to minimize the errors caused by at least some variations in water and bottom optical properties, and, in general, the larger the number of bands employed, the larger the range of variations can be tolerated. In our case, we choose the coefficients empirically, so as to minimize the difference between the estimated depth and the actual or *in situ* measurement of the depth for a large number of points. That is, we choose the h_j parameters to minimize the error

$$\varepsilon = \frac{1}{2} \sum_{m} \left\{ h^{(m)} - h_o + \sum_{j=1}^{N} h_j X_j^{(m)} \right\}^2 \tag{14}$$

where $h^{(m)}$ is the measured depth at sample location m and $X_j^{(m)}$ is the log-transformed radiance at this location. This minimization is accomplished by solving the set of equations

$$\frac{\partial \varepsilon}{\partial h_j} = 0, \qquad \text{for } j = 0, \ldots, N. \tag{15}$$

The parameters resulting from this procedure presumably minimize the errors due to the variations in the water-attenuation coefficients and bottom reflectance in the scenes used for "training" the algorithm. However, we find that these parameters are surprisingly universal in the sense that they can be applied to a large range of data sets while maintaining relatively small depth errors. These results will be discussed in more detail in Section VI below.

V. Data Sets

The data sets used in this paper include the IKONOS images indicated in Table I, along with corresponding ground-truth bathymetric measurements. Ground-truth bathymetry included LIDAR measurements from the SHOALS system [4], [10] for the Cancun and Hawaii data sets, detailed surveys of the near-shore bathymetry near Duck, NC, by the staff of the U.S. Army Corps of Engineers (USACE) field research facility [11], and digital bathymetry files compiled by the National Oceanographic and Atmospheric Administration (NOAA) for Carysfort Reef.

The bathymetry data sets were registered using a second-order bipolynomial (quadratic) fitting of the geographic coordinates (latitude, longitude) of the bathymetry data to the

TABLE I
IKONOS DATA SETS USED IN THIS STUDY

Site Name	Image Date	Solar Azimuth (deg T)	Solar Zenith (deg)	View Azimuth (deg T)	View Zenith (deg)
Cancun	6/9/2001	80.3	18.7	6.5	19.5
Duck, NC	7/3/2002	129.5	19.2	194.7	13.4
Kahana Bay, HI	1/9/2002	155.9	47.1	304.3	17.2
Carysfort Reef, FL	10/15/2000	146.5	39.5	132.4	25.1
Pearl Harbor, HI	7/17/2000	85.7	23.8	14.6	22.4
Honolulu, HI	3/21/2001	129.2	30.7	161.5	11.9
Diamond Head, HI	3/21/2001	128.9	30.9	28.4	20.9
Maunaloa Bay, HI	2/6/2000	139.5	46.9	59.1	2.8

line-element pixel locations of the imagery. This transformation was determined by using a set of 100 and 200 ground-control points consisting of the image coordinates (line and element numbers) of recognizable features along with the corresponding geographic coordinates of these features as obtained from navigational charts.

For each study site, the spatially transformed bathymetric measurements were allocated to the appropriate image pixel locations. If more than one depth value was assigned to a particular imagery location, the values within that cell were averaged. In the final step before analysis, each resulting image of bathymetric point values was linearly interpolated by panelizing the data using Delaunay triangulation in order to obtain a smooth and continuous representation of each site's bathymetry. The final stage of this process was to apply a correction to the ground truth to account for the tide height at the time of the IKONOS data collection.

Prior to the depth estimation, several preprocessing steps were applied to the data. First, the data were radiometrically calibrated to entrance aperture spectral radiance (EASR) using coefficients provided by Space Imaging [12]. Second, a 3×3 contraction of the images was done to reduce noise while maintaining an acceptable spatial resolution. Third, the images were segmented into three categories: 1) land/clouds; 2) deep water; and 3) shallow water, as described below. Fourth, the sun-glint correction described in Section III was applied, and finally, the mean radiance was estimated over optically deep water.

To segment the images, the NIR band is thresholded at $L = 2.5$ mW/cm$^2 \cdot$ sr $\cdot \mu$m. Breakers and clouds are also included in the nonwater category using this threshold. For the purpose of defining a water mask, this is exactly what we want since we will not be able to produce valid bathymetry estimates over areas where the bottom-reflected radiance is obscured by these effects. After the threshold is applied, the resulting binary image is clustered to identify small water regions (or holes) that are clearly not part of the coastal water body. These holes are "filled" by masking them out. This process helps to correct for terrain shadows as well as small ponds that are not the focus of the bathymetry process and may not have the same optical properties as the nearby ocean or sea. Note that if one intends to apply this algorithm to a small lake or pond, this process will likely mask out the lake. The size threshold currently used is 0.25 km^2; however, this value can be changed for inland lake applications.

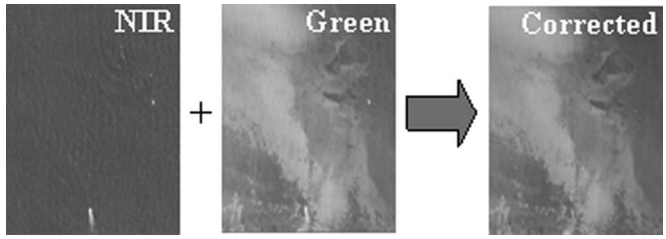

Fig. 1. Example of sun-glint-correction procedure applied to a subset of the Cancun image.

The second stage of the image segmentation procedure is to separate optically deep from shallow water. A first estimate of the mean deep-water radiance is calculated by first identifying the tenth-percentile brightness magnitude (using all four bands) within the water area of interest. A moving window is then passed through the image to identify kernels that contain more than 50% of pixels at or below the 10% brightness threshold. These kernels are designated deep-water regions and contribute to the calculation of the deep-water mean radiance and standard deviation of radiance in each band.

Once this process is complete, the blue and green bands are thresholded at the deep-water mean radiance plus three standard deviations. If the radiance of both the green and blue bands exceed their respective thresholds, the pixel is termed a shallow-water pixel. If not, the pixel is added to the deep-water category.

Having identified deep-water areas, the procedure discussed in Section III can be applied in order to reduce sun-glint effects. The result of applying this correction is illustrated in Fig. 1 for a subset of the Cancun image. There is significant variation in the NIR channel and this variation also appears in the green channel. After applying the correction in (6), most of this variation has been removed. Note that the ship wake in the lower part of the image is also largely removed from the image.

VI. BATHYMETRY PROCESSING AND RESULTS

To derive the coefficients in (9), five data sets having a solar zenith angle less than 30° (solar elevation $> 60°$) were used. Training areas were taken throughout the imagery wherever the bottom was clearly visible in both the green and blue bands (i.e., those classified as shallow-water areas, as discussed in the previous section). In order to account for variations in the solar zenith and observation angles, the coefficients α_j in (12) were modeled as

$$\alpha_j = \kappa_j \left[\sec \theta'_{\mathrm{s}} + \sec \theta'_{\mathrm{v}}\right] \tag{16}$$

where θ'_{s} is the solar zenith angle and θ'_{v} is the nadir view angle below the water surface. The least squares fitting procedure

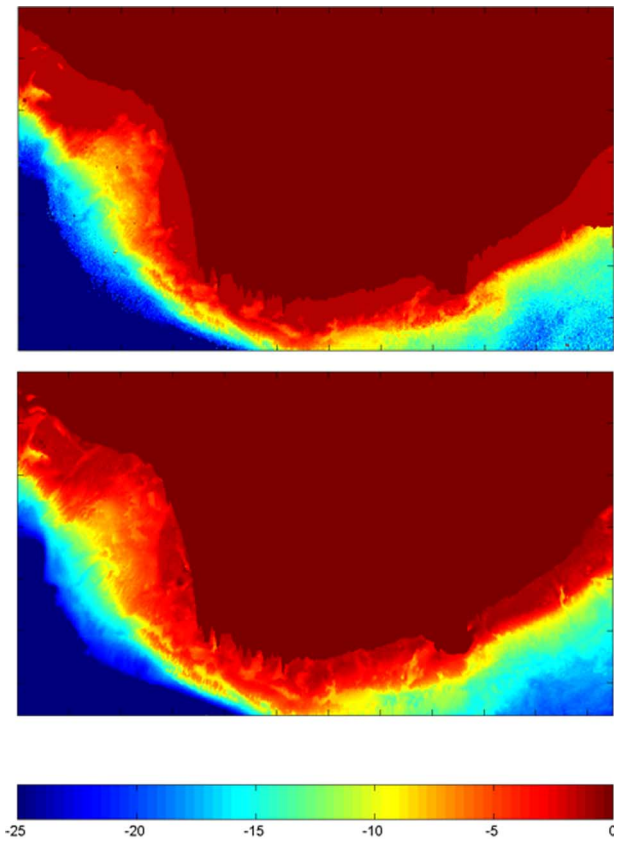

Fig. 2. Maps of estimated depth (upper panel) and ground-truth depth (lower panel) for the Diamond Head data set.

discussed in Section IV was then applied, resulting in the coefficients

$$h_0 = \frac{17.84 \text{ m}}{\sec\theta'_s + \sec\theta'_v} \tag{17}$$

$$h_1 = \frac{-17.42 \text{ m}}{\sec\theta'_s + \sec\theta'_v} \tag{18}$$

$$h_2 = \frac{26.7 \text{ m}}{\sec\theta'_s + \sec\theta'_v} \tag{19}$$

where the subscript 1 refers to the IKONOS blue band, and 2 refers to the green band. These coefficients were then used to calculate the depths for all of the remaining shallow-water data points. Examples of the depth maps obtained from this procedure are shown in Figs. 2 and 3 for Diamond Head, Hawaii, and Cancun, Mexico. The depths estimated from the IKONOS data are shown in the upper panel of each figure, and the ground-truth depths are shown in the lower panels.

The estimated depths are plotted versus the ground-truth depths for each of the data sets in Figs. 4–11. These plots were generated by binning the estimated depths by the ground-truth depths. Bins having a number of samples less than half the average number of samples per bin were neglected, and the populations of the remaining bins were equalized so as to give each depth interval the same weight. The mean and root mean square (rms) errors for each data set are shown on the plots. The errors were reduced considerably by correcting for solar and view-angle effects, as indicated in (17)–(19), although

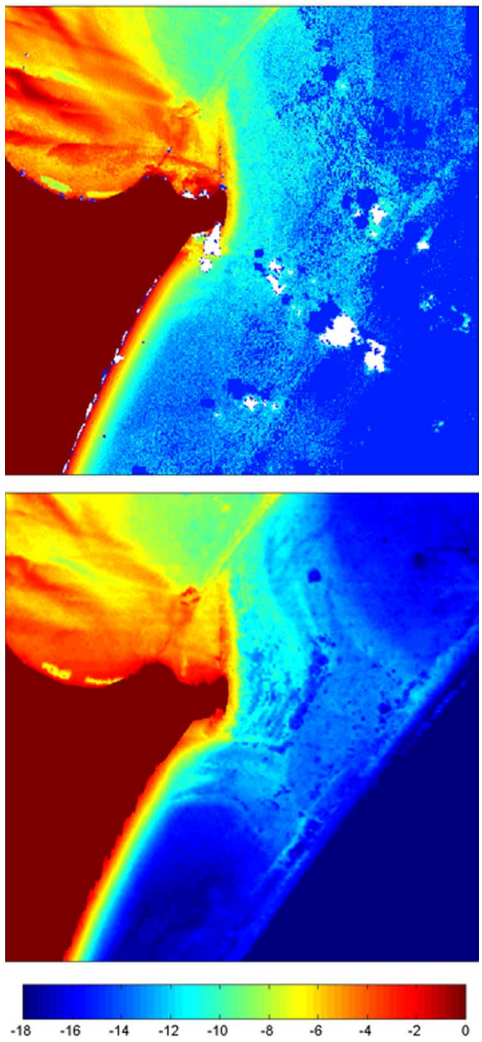

Fig. 3. Maps of estimated depth (upper panel) and ground-truth depth (lower panel) for the Cancun data set.

significant biases remain in several of the data sets. The rms errors for each data set are plotted versus the solar zenith angle in Fig. 12, along with the results obtained by scaling each data set individually so as to minimize the rms error. The aggregate rms error over all data sets is 2.3 m using (17)–(19), and 1.7 m using the individually scaled data sets.

VII. Discussion

The results presented in the previous section indicate that the depth algorithm appears to compensate to some extent for the variations in water optical properties and/or bottom reflectance that are presumed to exist within each data set and among the different data sets.

To gain further insight into the algorithm performance over variable bottom and water properties, consider the scatter plots shown in Figs. 13–15. Fig. 13 shows the log-transformed signals in the blue and green bands plotted versus the ground-truth depth for a set of points selected from the lower part (lines 450–500) of the Cancun data set shown in Fig. 3, with depths ranging from 4 to 12 m. From the tightness of the scatter,

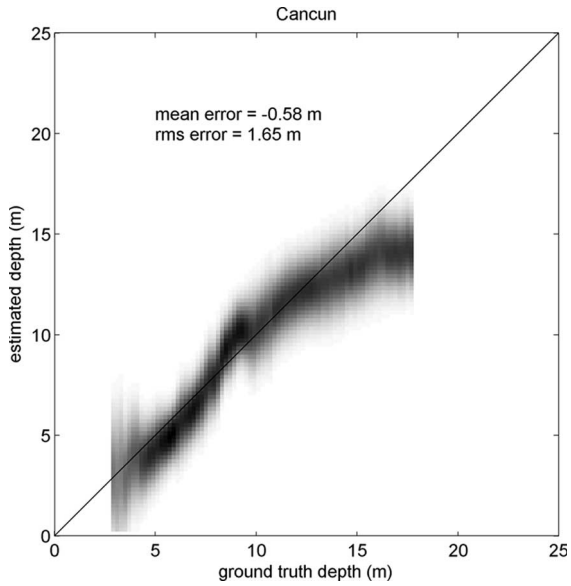

Fig. 4. Estimated depth versus ground truth for the Cancun data set.

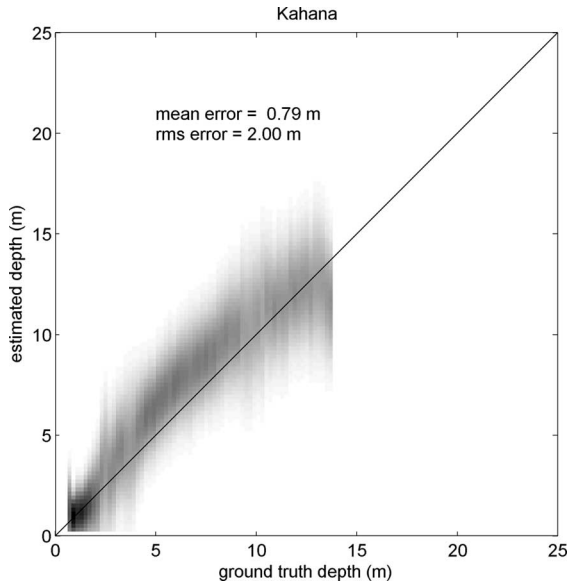

Fig. 6. Estimated depth versus ground truth for the Kahana data set.

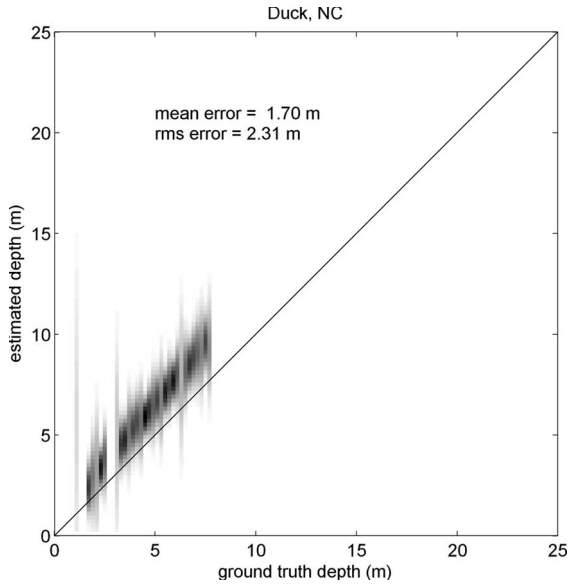

Fig. 5. Estimated depth versus ground truth for the Duck, NC, data set.

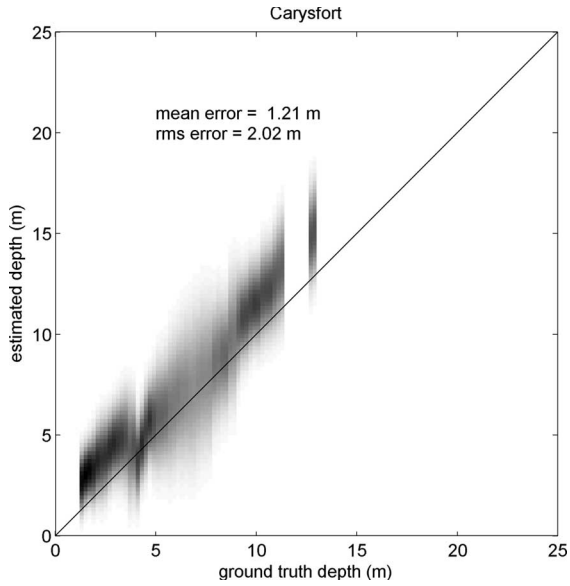

Fig. 7. Estimated depth versus ground truth for the Carysfort data set.

it appears that the bottom reflectance and the water-attenuation coefficients were both fairly uniform for this set of points. A least squares fit yields diffuse attenuation coefficients of 0.056 and 0.074 m^{-1} in the blue and green bands, respectively.

Fig. 14 shows a scatter plot of the log-transformed signals in the green band versus those in the blue band, for a set of points taken from the upper part (lines 200–250) of the Cancun image. Different symbols are used for points in the depth ranges from 2–4, 6–8, and 10–12 m. Clearly, there is a wide variation of the signals within each of these depth intervals, which could be caused by variations in either the water optical properties or the bottom composition. We first consider the hypothesis that these variations are due to changes in the water-attenuation coefficient.

As discussed in Section IV, the form of the depth algorithm (9) is such that variations in the water-attenuation coefficient have no effect on the calculated depth if these variations are caused by constituents whose specific attenuation coefficients satisfy (13). For the parameters shown in (17)–(19), this condition implies that $\alpha_1^*/\alpha_2^* = 1.53$. Qualitatively, the condition $\alpha_1^*/\alpha_2^* > 1$ is expected for constituents such as chlorophyll or dissolved organic matter, which absorb more in the blue than in the green region of the spectrum [13]. As an example, assume that the specific attenuation coefficients in the blue and green bands are $\alpha_1^* = 0.015\ \mathrm{m}^2 \cdot \mathrm{mg}^1$ and $\alpha_2^* = 0.010\ \mathrm{m}^2 \cdot \mathrm{mg}^{-1}$. The values of the parameter α in (2) are then given by $\alpha_1 = 2K_1 + \alpha_1^* C$, and $\alpha_2 = 2K_2 + \alpha_2^* C$, where K_1 and K_2 are the water-attenuation coefficients shown in Fig. 13, and C is the concentration of the variable constituent. The radiances calculated from (2) using these values are indicated by the solid lines in Fig. 14 for various depths and for values of C ranging from 0 to 10 $\mathrm{mg/m}^3$. There is a fair agreement

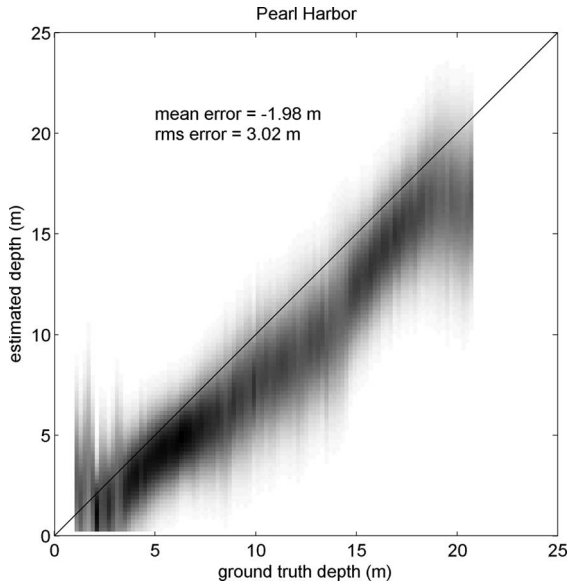

Fig. 8. Estimated depth versus ground truth for the Pearl Harbor data set.

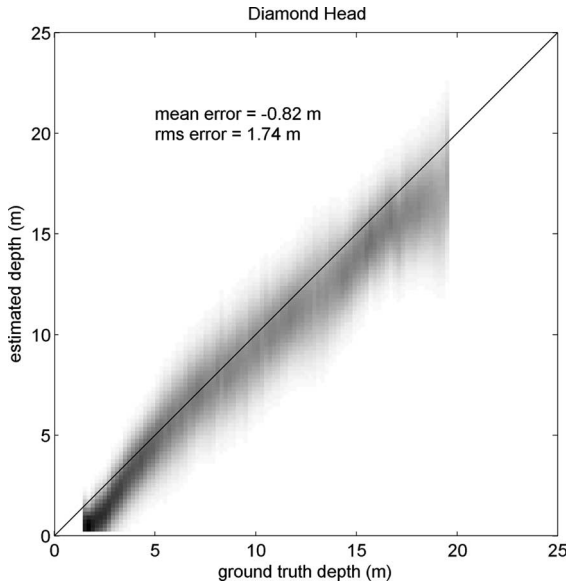

Fig. 10. Estimated depth versus ground truth for the Diamond Head data set.

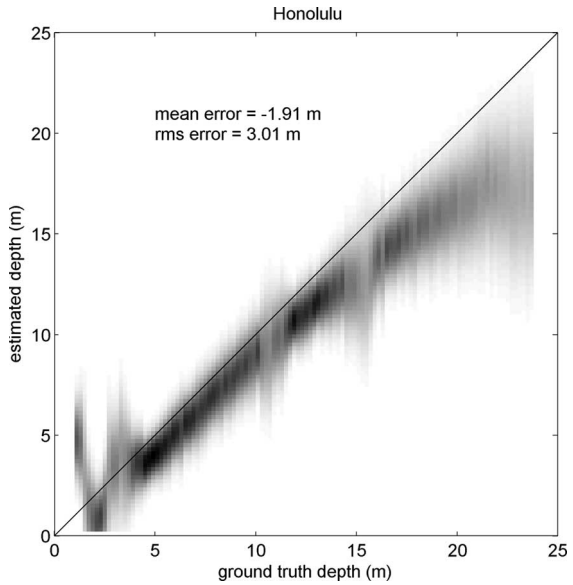

Fig. 9. Estimated depth versus ground truth for the Honolulu data set.

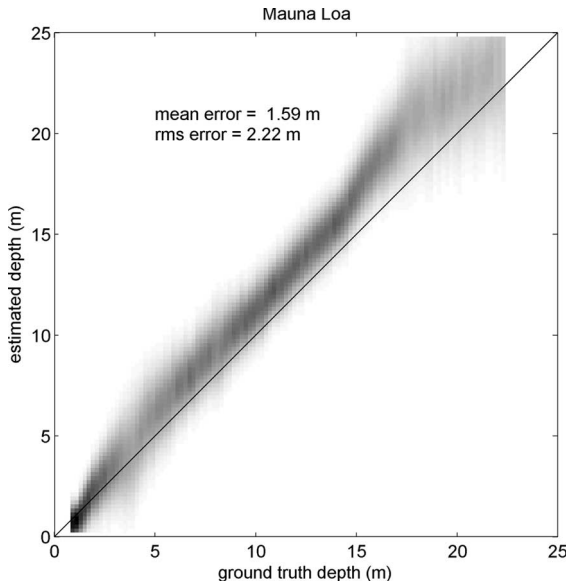

Fig. 11. Estimated depth versus ground truth for the Mauna Loa data set.

between the calculated and observed signals in the sense that most of the data points fall between the lines corresponding to the calculations for the appropriate depth limits. Thus, it is possible to conclude that the observed variability is due to water-attenuation variations as modeled above.

The alternative hypothesis that the observed variability is due to changes in the bottom reflectance is illustrated in Fig. 15. This figure shows the same set of data points, but the solid curves in this case indicate lines of constant depth, as calculated from the reflectance model using the water-attenuation coefficients shown in Fig. 13 and a bottom reflectance given by a mixture of sand and vegetation. Specifically, the factor L_{b} in (2) was assumed to be given by

$$L_{\mathrm{b}} = L_{\mathrm{sand}} f_{\mathrm{sand}} + L_{\mathrm{veg}}(1 - f_{\mathrm{sand}}) \tag{20}$$

where $L_{\mathrm{sand}} = 12.2$ mW/cm$^2 \cdot$ sr $\cdot\, \mu$m in both bands, $L_{\mathrm{veg}} = 0.4$ mW/cm$^2 \cdot$ sr $\cdot\, \mu$m in band 1 and 1.2 mW/cm$^2 \cdot$ sr $\cdot\, \mu$m in band 2, and $0 < f_{\mathrm{sand}} < 1$ is the fraction of the bottom covered by sand. This model fits the data points better than the lines shown in Fig. 14, indicating that the variability observed in this case is probably due to bottom-reflectance variations. It is interesting to note, however, that the water-depth decision boundaries for the two cases are fairly similar. Thus, the depth algorithm expressed by (9), with the parameters shown in (17)–(19), appears to be capable of correcting for at least some range of bottom reflectance as well as water optical-property variations.

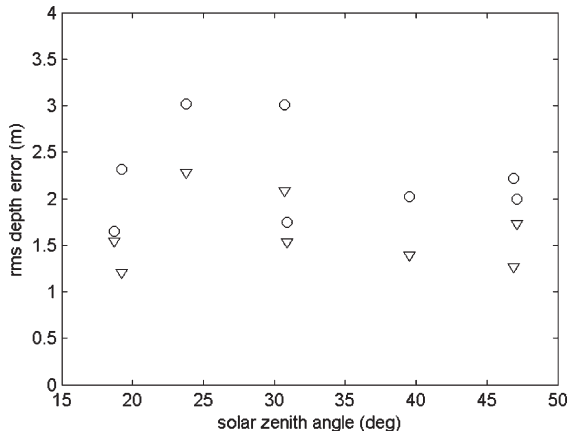

Fig. 12. RMS depth errors for each data set using (circles) a physically based algorithm and (triangles) using empirical correction factors based on ground-truth measurements.

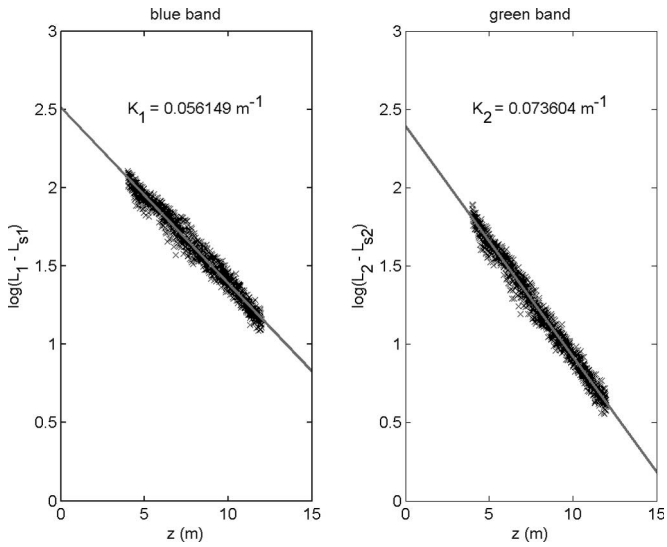

Fig. 13. Scatter plots of blue and green signals versus depth for a subset of the Cancun image in which the water and bottom optical properties appear to be uniform.

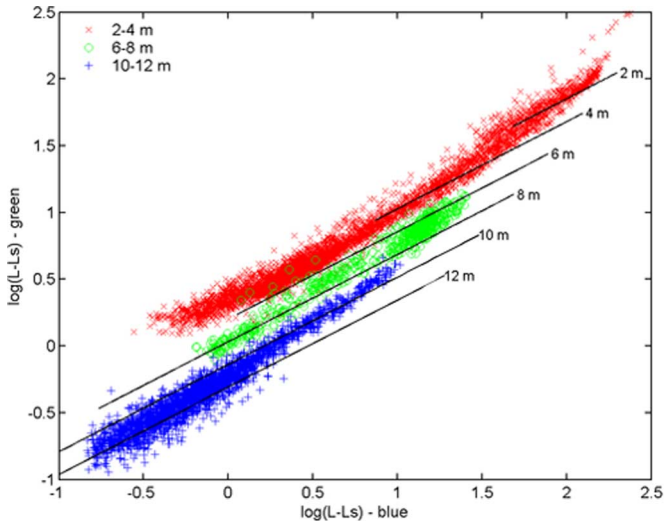

Fig. 14. Scatter plot of green versus blue signals for a second subset of the Cancun image containing variations in the bottom reflectance and/or the water-attenuation coefficient. Solid lines indicate radiances calculated for variable-attenuation coefficients, as discussed in the text.

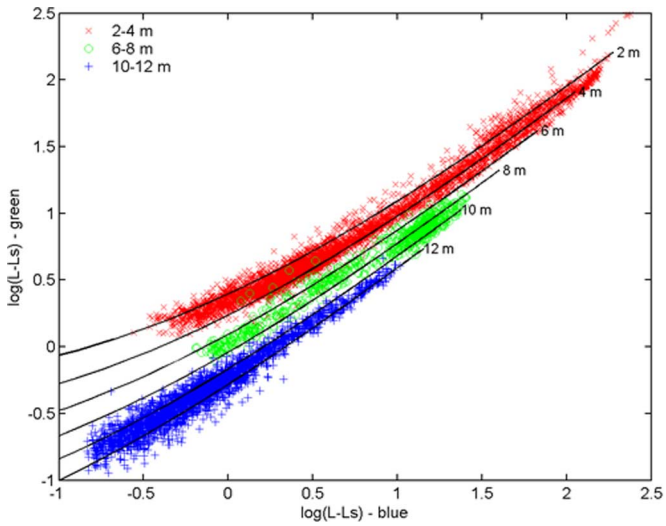

Fig. 15. Scatter plots of green versus blue signals for the same subset as shown in Fig. 14, compared with the signals computed by assuming that the bottom reflectance is a mixture of sand and vegetation.

VIII. Summary and Conclusion

This paper describes a simple method of estimating water depths from multispectral imagery, based on an approximate shallow-water reflectance model. A single set of coefficients derived from a set of IKONOS images produces good performance over a variety of conditions, with an aggregate rms error of 2.3 m over all of the data sets. The algorithm corrects for a range of variations in both water attenuation and bottom reflectance using a linear combination of the log-transformed radiances in the blue and green channels. A comparison of the observed radiances with model predictions illustrates how these corrections are made.

References

[1] R. P. Stumpf, K. Holderied, and M. Sinclair, "Determination of water depth with high-resolution satellite imagery over variable bottom types," *Limnol. Oceanogr.*, vol. 48, no. 1, pp. 547–556, 2003.

[2] J. C. Sandidge and R. J. Holyer, "Coastal bathymetry from hyperspectral observations of water radiance," *Remote Sens. Environ.*, vol. 65, no. 3, pp. 341–352, Sep. 1998.

[3] Z. Lee, K. L. Carder, C. D. Mobley, R. G. Steward, and J. S. Patch, "Hyperspectral remote sensing for shallow waters: 2. Deriving bottom depths and water properties by optimization," *Appl. Opt.*, vol. 38, no. 18, pp. 3831–3843, Jun. 1999.

[4] W. J. Lillycrop, J. L. Irish, and L. E. Parson, "SHOALS system," *Sea Technol.*, vol. 38, no. 6, pp. 17–25, 1997.

[5] H. R. Gordon, "Simple calculation of the diffuse reflectance of the ocean," *Appl. Opt.*, vol. 12, no. 12, pp. 2803–2804, 1973.

[6] D. R. Lyzenga, "Passive remote sensing techniques for mapping water depth and bottom features," *Appl. Opt.*, vol. 17, no. 3, pp. 379–383, Feb. 1978.

[7] W. D. Philpot, "Bathymetric mapping with passive multispectral imagery," *Appl. Opt.*, vol. 28, no. 8, pp. 1569–1578, Apr. 1989.

[8] Z. Lee and K. L. Carder, "Effect of spectral band numbers on the retrieval of water column and bottom properties from ocean color data," *Appl. Opt.*, vol. 41, no. 12, pp. 2191–2201, Apr. 2002.

[9] D. R. Lyzenga, "Shallow-water bathymetry using combined LIDAR and passive multispectral scanner data," *Int. J. Remote Sens.*, vol. 6, no. 1, pp. 115–125, 1985.
[10] G. C. Guenther, M. W. Brooks, and P. E. LaRocque, "New capabilities of the SHOALS airborne LIDAR bathymeter," *Remote Sens. Environ.*, vol. 73, no. 2, pp. 247–255, Aug. 2000.
[11] U.S. Army Corps of Engineers Field Research Facility Online Data. [Online]. Available: http://www.frf.usace.army.mil/frfdata.html
[12] Space Imaging Corporation, IKONOS Relative Spectral Response and Radiometric Calibration Coefficients, (2004). [Online]. Available: http://www.spaceimaging.com/products/ikonos/spectral.htm
[13] A. Bricaud, M. Babin, A. Morel, and H. Claustre, "Variability in the chlorophyll-specific absorption coefficients of natural phytoplankton: Analysis and parameterization," *J. Geophys. Res.*, vol. 100, no. C7, pp. 13321–13332, Jul. 1995.

David R. Lyzenga received the B.S.E. degree in engineering physics from the University of Michigan, Ann Arbor, in 1967, the M.S. degree in physics from Yale University, New Haven, CT, in 1968, and the Ph.D. degree in electrical engineering from the University of Michigan, in 1973.

He worked at the Environmental Research Institute of Michigan from 1974 to 1987, and was an Associate Professor in the College of Marine Studies at the University of Delaware from 1987 to 1989. He presently holds joint research appointments at the University of Michigan and the General Dynamics Advanced Information Systems Division, Ann Arbor. His research interests include interactions of electromagnetic radiation with the ocean, and remote sensing of the ocean using both radar and optical techniques.

Norman P. Malinas received the B.S.E. and M.S.E. degrees in electrical engineering from the University of Michigan, Ann Arbor, in 1987 and 1992, respectively. His M.S.E. study was on signal processing.

He has worked at the Environmental Research Institute of Michigan (now General Dynamics Advanced Information Systems Division) since 1985, as a Research Engineer. His research interests include physical-information estimation and feature extraction from remotely sensed imagery using both radar and optical techniques.

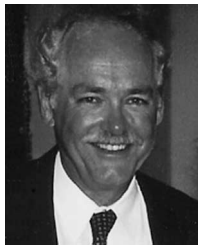

Fred J. Tanis received the B.S. and M.S. degrees in mathematics from the University of Michigan, Ann Arbor, in 1964 and 1966, respectively.

He worked at the Environmental Research Institute of Michigan from 1972 to 2002. He presently works as a Consultant on optical sensors and techniques.